The dynamical origin of subduction zone topography

H. J. Melosh and Arthur Raefsky *Division of Geological and Planetary Sciences, California Institute of Technology, Pasadena, California 91125, USA*

Summary. Subduction zones are expressed topographically by long linear oceanic trenches flanked by a low outer rise on the seaward side and an island arc on the landward side. This topographic structure is reflected in free air gravity anomalies, suggesting that much of the topography originates from dynamical forces applied at the base of the crust. We have successfully reproduced the general topographic features of subduction zones by supposing that the stresses generated by the bending of the viscous lower lithosphere as it subducts are transmitted through the thin elastic upper portion of the lithosphere. The trench is due to a zone of extensional flow (associated with low pressure) in the upper part of the viscous lithosphere.

The stresses in the subducting slab are computed using a finite element technique, assuming a Maxwell viscoelastic constitutive relation. Various dips (10 to 90°) were investigated, as well as depth dependent and non-Newtonian (power law, $n = 3$) viscosities. Observed subduction zone dimensions are well reproduced by these models. The effective viscosity required at mid-depth in the lithosphere is about 6×10^{22} P. This low value is probably due to the stress dependence of the effective viscosity. However, these models also show that the topography of the subduction zone depends primarily upon the geometry of the subducting slab (dip, radius of curvature of the bend) rather than upon its rheology. Shear stresses beneath the trench reach maxima of approximately 50 MPa. An interesting feature of some solutions is a dynamically supported bench or platform between the trench and island arc.

1 Introduction

The large scale topography and free air gravity profiles of subduction zones are nearly universal. Virtually every one of the Earth's subduction zones is expressed by a deep linear or gently curved trench 1.5–5 km deep, 100–200 km wide, and up to 5000 km in length. This trench is flanked by a topographic high which rises 2–4.5 km above the mean level of

the seafloor. The high is not as regular as the trench, since it may consist of either continental crust or an island arc. Seaward of the trench a low topographic rise, the 'outer rise', is commonly found. This broad rise crests about 100 km from the trench axis and is never more than 500 m high.

Hayes & Ewing (1970, Fig. 19) plotted 35 projected topographic profiles of subduction zones, aligning only the trench axes. This plot, in which vertical and horizontal dimensions were not normalized, shows that the different trench profiles roughly define a single, universal, curve.

This similarity of topography also extends to free air gravity anomalies (Hayes & Ewing 1970; Watts & Talwani 1974). The outer rise is associated with $+50$ to $+80$ mgal free air gravity anomalies, the trench has from -200 to -350 mgal anomalies, and the island arc or continental margin adjacent to the trench shows $+50$ to $+250$ mgal anomalies. The width of the positive anomaly associated with the continental margins or island arc is about the same as the width of the trench. This anomaly is nearly an inverted image of the trench anomaly, in contrast to the topographic profile for which the correspondence is less exact. Fig. 1 shows these relations schematically.
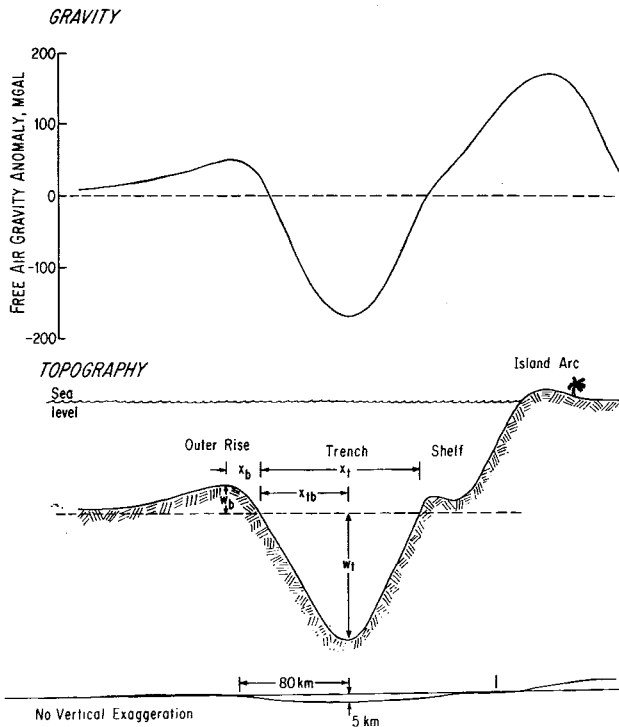

Figure 1. Schematic cross section of a typical subduction zone, showing a highly exaggerated outer rise, height w_b, with crest posistioned a distance x_b from the outer trench wall's intersection with the level of undeflected seafloor (dashed line). The trench's depth is w_t, total width x_t, and the distance from the trench axis (the deepest part of the trench) to the outer wall's intersection with the level of undeflected seafloor is x_{tb}. The difference between x_{tb} and $x_t/2$ is a measure of the trench's asymmetry. The bench which develops for the circular arc velocity profiles is shown schematically, along with the island arc high. The topography of a subduction zone is reflected in the free air gravity anomaly profile, sketched above. At the bottom of the figure is a cross section of the subduction zone with no vertical exaggeration, showing that in reality surface dips are very small and that the deflection of the lithosphere in the trench is much less than the $c.$ 100 km thickness of the lithosphere. This deflection can thus be neglected in computing the flow field due to bending of the subducted slab.

The similarity of both topographic and free air gravity profiles for nearly all subduction zones strongly suggests that a single process acts to produce these features. The existence of large free air anomalies further suggests that this process is dynamic: forces generated during subduction act on the surface of the Earth to produce the observed topography.

In this paper we propose that these forces are due to viscous stresses generated by the bending of the oceanic lithosphere as it is subducted. The lithosphere is treated as a two-layer composite: an elastic layer 15–30 km thick overlies a highly viscous layer 50–80 km thick. This model accords with the observations of Walcott (1970), Watts, Cochran & Selzer (1975), Watts (1978) and McNutt & Menard (1978) on the flexural rigidity of the oceanic lithosphere for loads of more than a few Myr duration (which is the mechanical time-scale for subduction). Beneath the lithosphere the asthenosphere is a layer of especially low effective viscosity (10^{19}–10^{21} P) which probably decouples the lithosphere from the mantle below (Elsasser 1969).

As the lithosphere subducts and bends downward, extensional flow in the upper part of the very viscous lower layer produces a low pressure zone. This low pressure zone is the source of the topographic low that we recognize as an oceanic trench. (Similarly, a high pressure zone produces a topographic and free air gravity high.) To see how a low pressure zone in the lithosphere results in a trench, first imagine a simplified situation in which there is no water in the ocean basin. In this case, the top of the lithosphere must be a surface of zero normal (and tangential) forces – a free surface. Since the flow is quasi-static, and inertial forces are negligible, the development of a zone of low pressure beneath the crust must be compensated by a decrease in thickness of the overlying rock (and associated lithostatic pressure) large enough to balance the pressure decrease at depth:

$$\Delta h = \Delta P / \rho_c g \qquad\qquad (1)$$

where Δh is the increase in the depth of the sea floor, ΔP is the decrease in pressure at the base of the crust, ρ_c is crustal density and g is the acceleration of gravity. This increase in depth insures that there is no net normal force at the surface. When seawater is present the effective density of the crust is $(\rho_c - \rho_w)$, where ρ_w is the density of seawater. Otherwise, the results are the same in the presence of seawater as without it.

This argument relating pressure (or stress) at the base of the crust to topography is approximate. It neglects the ability of the elastic part of the lithosphere (the upper 15–30 km) to transmit normal forces to moderate distances. The effect of the elastic lithosphere is much like a filter: deflections due to normal forces with wavelengths much longer than a cut-off wavelength (given by the flexural parameter, α) are transmitted through the lithosphere essentially unaltered. Deflections due to shorter wavelength forces are smoothed and averaged (Officer 1974). The observed flexural parameter of the oceanic lithosphere is between 40 and 75 km (Walcott 1970; Watts *et al.* 1975; McNutt & Menard 1978). Oceanic trenches, characterized by distance scales of 100 km or more, are thus not strongly influenced by the elastic part of the lithosphere.

The elastic lithosphere's difficulty in supporting loads with wavelengths comparable to oceanic trenches is epitomized by the large fibre stresses required to explain the outer rise on the basis of elastic flexure models (Hanks 1971). Much smaller stresses are obtained if it is assumed that the outer rise is due to viscous stresses generated in the lower part of the lithosphere and transmitted nearly unaltered to the surface (Melosh 1978). Flexure of the elastic lithosphere may account for some percentage of the surface deformation, and may modify somewhat the deflections due to forces generated at the top of the viscous lower lithosphere, but the dominant effects must be due to deep-seated viscous forces. Although the elastic lithosphere does bend sharply during subduction, and would certainly develop multi-kilobar internal stresses if it were perfectly elastic, the observation of many normal

faults on the outer trench walls (Jones *et al.* 1979) and the observed seismicity (Chapple & Forsyth 1979) suggest that the elastic lithosphere fractures at stress levels less (and perhaps much less) than a kilobar. Since much larger surface extensional stresses than this are necessary to support the entire outer rise elastically, viscous stresses must make up the difference. For example, if the elastic lithosphere can support no more than a few hundred bars of differential stress (Chinnery 1964), then less than 10 per cent of the outer rise height can be due to elastic bending stresses. In our model, such elastic stresses do not need to be present at all: the model would work perfectly if the lithosphere were a flexible, but inextensible, sheet. For the purpose of this paper, we assume that elastic bending stresses are unimportant.

This assumption is further supported by the observation of normal faulting earthquakes which extend to 70 km depth in the oceanic plate (Kanamori 1971; Stewart 1978). Since the lower half of a flexed elastic plate 30 km thick is in compression, such events appear to rule out flexure of the elastic lithosphere as a major contributor to the topography of the outer rise.

In this paper we focus on the viscous lower lithosphere. The elastic upper part of the lithosphere is treated approximately (it applies a constant velocity boundary condition), as is the asthenosphere below (it is treated as a decoupling zone). Forces due to density differences are included implicitly, as part of the boundary condition. We thus compute the stresses in the subducting lithosphere due to bending alone, and evaluate these stresses on its upper surface. We show that these stresses result in a deflection of the lithosphere of the correct shape and size to explain the oceanic trench, the outer rise, and part of the island arc (which we postulate is due to high pressures developed in the unbending portion of the lithosphere and transmitted to the surface through the overlying complex of upper mantle and crustal rocks). We aim to explain only the first order topographic features: trench, outer rise and island arc, hence we neglect the shorter wavelength response of the elastic lithosphere. Although we thus expect deviations in detail from the results presented in this paper, we believe that the general conclusions are correct.

To implement even this limited goal, we found it necessary to employ numerical methods. A finite element code, constructed especially for tectonic problems, is used to compute the stresses and deformation in a lithospheric slab subducting at various angles with either constant Newtonian viscosity, depth dependent Newtonian viscosity, or constant non-Newtonian ($n = 3$) viscosity.

These complex numerical models are not, however, necessary to obtain an order of magnitude estimate of the effective viscosity in the lower lithosphere. The stress on the base of the lithosphere is given roughly by $\Delta P = 2\eta_{\text{eff}}\dot{\epsilon}$, where $\dot{\epsilon}$ is a representative strain rate; $\dot{\epsilon}$ is approximately the change in velocity of the slab during subduction, $v \sin\theta$, divided by the lithosphere thickness, H. v is the convergence velocity and θ the dip of the slab. Since the stress ΔP is related to the topography by equation (1), we have

$$\eta_{\text{eff}} \simeq \frac{(\rho_{\text{c}} - \rho_{\text{w}})gH\Delta h}{2v \sin\theta} \tag{2}$$

Taking $\Delta\rho = 1.7 \text{ gm cm}^{-3}$, $g = 980 \text{ cm s}^{-2}$, $\Delta h = 4.5 \text{ km}$, $H = 70 \text{ km}$, $v = 70 \text{ mm yr}^{-1}$, and $\theta = 45°$, we find $\eta_{\text{eff}} \simeq 2 \times 10^{22} \text{ P}$. Although this viscosity seems somewhat low for mid-depth in a Newtonian lithosphere, a non-Newtonian rheology makes this plausible, since the deviatoric stresses near the bend axis reach several hundred bars.

2 Boundary conditions for the model

The stresses and flow field in the viscous lower lithosphere can be computed only after appropriate boundary conditions are specified. Earthquake locations define the geometry

of the downdipping slab after it is subducted. It is reasonable to assume that, in a coordinate frame in which the bend axis is fixed, the velocity of the subducted slab is the same as the plate before subduction (especially above 700 km where earthquakes attest to the rigidity of a portion of the lithosphere). This assumption is supported by the approximate (*c.* 10 per cent) agreement between subduction rates estimated from seismic moment sums (Davies & Brune 1971) and rates estimated from rigid plate tectonics. The top of the viscous part of the lithosphere is thus subject to kinematic, or velocity, boundary conditions. These boundary conditions are enforced by the overlying elastic lithosphere. The resistance of the elastic lithosphere to compression or extension constrains the velocity to be nearly constant and tangent to the surface of the lithospheric slab. The elastic lithosphere imposes this constraint by exerting forces on the viscous lower lithosphere. Long wavelength normal forces are transmitted through the lithosphere nearly unchanged. These forces are balanced by topography on the Earth's surface. Tangential forces are converted to compressional or extensional stresses in the elastic lithosphere. If the shear stress on the base of the elastic lithosphere is $\sigma_{xz}^{b}(x)$, and the upper surface is free ($\sigma_{xz} = 0$), then a stress σ_{xx}^{el} must appear in the elastic layer (see Melosh 1977, for a derivation)

$$\sigma_{xx}^{el} = \frac{1}{T} \int_{\infty}^{x} \sigma_{xz}^{b}(x') \, dx' \qquad (3)$$

where T is the thickness of the elastic lithosphere. Once the slab is subducted σ_{xz} no longer vanishes on top of the elastic lithosphere. Stresses in the *elastic* lithosphere are thus indeterminate after subduction. However, we show below that so long as the elastic lithosphere continues to move at constant velocity, stresses in the *viscous* lithosphere are determined.

Velocity boundary conditions on one surface of the viscous lithosphere cannot determine the stress and velocity fields within it. Other boundary conditions are required. Such conditions are supplied by the asthenosphere beneath the lithosphere (we approximate these two regions as discrete layers, although they are likely to be gradational in their mechanical properties). The asthenosphere is a zone of low viscosity (10^{19}–10^{21} P) underlying the lithosphere. The stress it exerts on the base of the lithosphere is probably orders of magnitude less than the stress developed in the lithosphere at comparable strain rates. The boundary condition at the base of the lithosphere is thus well approximated by assuming it is free of shear stress and normal stress other than that due to hydrostatic pressure.

Note that hydrostatic stresses are not included in the following computations: they can always be added to the dynamic stresses, however, and do not influence the results in any way. The difference in density between the slab and the upper mantle appears as a normal force on the surface of the slab. This force must be exerted on the slab in order to maintain the assumed geometry. The present approach says nothing about the origin of this force: it presumably originates in the dynamics of flow in the mantle outside the slab (Sleep 1975). The object of this paper is to show that, regardless of such dynamical unknowns, the *geometry* and *rheology* of the bending slab *alone* determine the stresses in the slab, and hence the topography of the subduction zone.

The velocity and stress boundary conditions discussed above uniquely determine the stress and velocity fields everywhere in the viscous lower lithosphere (Batchelor 1970). It is not necessary to know anything about stresses exerted on the subducting slab by gravity, by the overthrust slab, or even by flow in the back-arc region: such forces do determine the geometry of the subducting slab, but since this is already known from earthquake locations, the stresses in the viscous part of the subducting slab can be computed. *Thus, kinematic boundary conditions derived from the observed geometry of the subducting slab completely*

determine the stress field in the lower lithosphere. This is fortunate for our purposes, since we can relate the topography and free air gravity of the subduction zone to the bending slab without having to work out the complete dynamics of flow in the mantle.

Even with these straightforward boundary conditions, and the limited goal of computing the stress and velocity fields in the viscous lower lithosphere, the complex boundary shapes and possible complex rheology of the lithosphere prevent exact analytic solutions. Melosh (1978) solved an approximate analytic model which assumed constant Newtonian viscosity and a planar lower boundary. Although the results of that study were encouraging, application to the Earth requires consideration of large dips (up to nearly 90° in the Mariana Trench), depth dependent viscosity, and non-Newtonian rheology (Weertman & Weertman 1975). These phenomena can only be studied numerically. We thus constructed a finite element model of the viscous lower lithosphere, bounded on top by the elastic lithosphere (represented by a velocity boundary condition; fixed velocities are applied at each top node point), and bounded on the bottom by a stress-free surface representing the asthenosphere.

Fig. 2 shows examples of the two finite element grids used in this investigation. Both are shown for 45° dip and a radius of curvature of $1.85\,H$ (H = slab thickness) at the bend axis. The grid in Fig. 2(a) is composed of three distinct parts: a horizontal rectangular grid, a section of a circle (actually a cylinder in three dimensions) and a rectangular grid dipping at 45°. Plane strain elements are used throughout, so we actually model an infinite length trench. The grid in Fig. 2(b) is constructed from an error function deflection described later. Its curvature changes continuously, unlike Fig. 2(a) which has zero curvature on the straight sections and constant curvature on the circular section. The slab dip and radius of curvature in the bend are varied in our calculations. The results depend strongly upon both parameters.

These grids are constructed so that a line of elements approximates a streamline of the flow (we work in a frame of reference fixed with respect to the bend so that the flow is steady). The grid remains fixed while velocity vectors are computed at the node points. It is not necessary that the sides of the elements be parallel to streamlines, but accuracy is
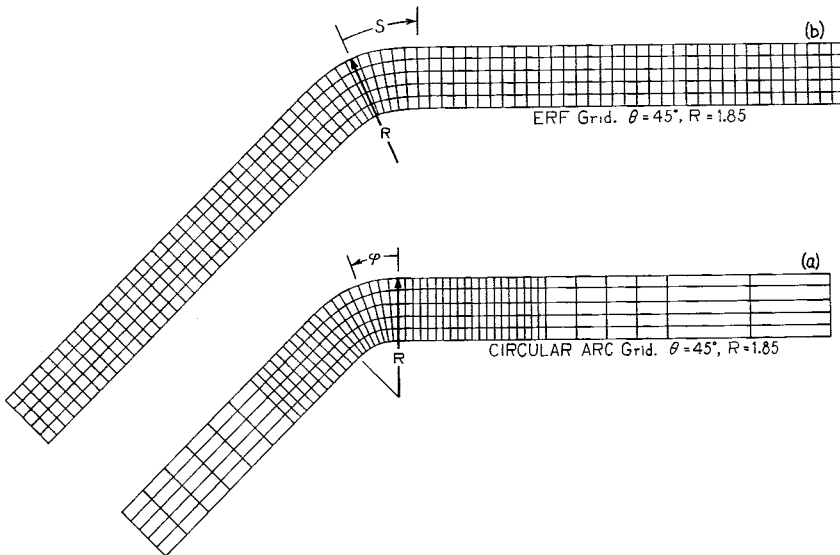

Figure 2. Finite element grids used in the numerical computations. The radius of curvature in the bend is R for both circular arc (a) and error function (b) grids. ϕ is the angle from the beginning of the bend in (a) and s is arc distance from the bend in axis in (b). A node point is located at the corners of each quadrilateral element.

higher if this occurs, especially when variable viscosity is used. Small components of flow into or out of the grid boundaries in the bend can develop without leading to serious errors.

The two grid types are associated with slightly different velocity fields. In both cases the velocity boundary conditions are applied so that the velocity vectors are nearly tangent to the grid. The simplest choice is to make the velocity vectors precisely tangent to grid 2a:

$$\left.\begin{array}{l} v_y = 0 \\ v_x = -v \end{array}\right\} \text{horizontal section}$$

$$\left.\begin{array}{l} v_y = -v \sin \phi \\ v_x = -v \cos \phi \end{array}\right\} \text{circular arc} \tag{4}$$

$$\left.\begin{array}{l} v_y = -v \sin \theta \\ v_x = -v \cos \theta \end{array}\right\} \text{dipping section}$$

where θ is the dip angle of the slab and ϕ is the angle between the beginning of the bend and the grid point at which the velocity is evaluated (Fig. 2(a)). v is the net convergence velocity in the subduction zone. The derivative of the velocity condition equation (4) is discontinuous at the beginning and end of the bend, leading to trouble when strain rates are evaluated (Fig. 3, curve a). We thus employ a smoothed velocity profile in the circular arc section (Fig. 3, curve b):

$$v_y = \begin{cases} -\dfrac{v \sin \phi}{2}\left[1 - \cos\left(\dfrac{2\pi\phi}{\theta}\right)\right]; & 0 < \phi < \theta/2 \\[4mm] -\dfrac{v \sin \phi}{2}\left[1 - \cos\left(\dfrac{2\pi\phi}{\theta}\right)\right] - \dfrac{v \sin \theta}{2}\left[1 + \cos\left(\dfrac{2\pi\phi}{\theta}\right)\right]; & \dfrac{\theta}{2} < \phi < \theta \end{cases}$$
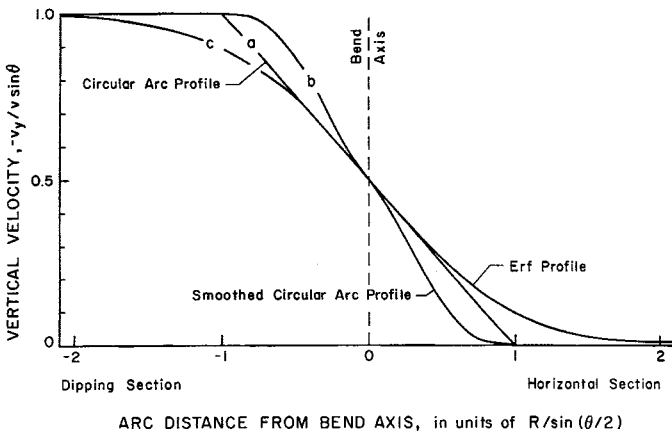
$$v_x = -\sqrt{v^2 - v_y^2}. \tag{5}$$

Figure 3. The vertical (downward) velocity component v_y as a function of arc distance from the bend axis. The horizontal velocity component v_x is chosen so that the total velocity is constant. Curve (a) velocity vectors are tangent to the circular arc grid (Fig. 2(a)). This profile has discontinuous derivatives at the ends of the circular arc section. Curve (b) is a smoothed version of profile (a) which has continuous derivatives. Curve (c) is the error function profile with velocity vectors tangent to grid (2b). These curves refer to a subduction zone with 10° dip. Curves (a) and (b) are slightly different for higher dips.

In order to compare the numerical results directly with the analytical results of Melosh (1978) and to study the effect of a slightly different geometry, we also investigate an error function velocity profile (Fig. 3, curve c):

$$v_y = -\frac{v \sin \theta}{2} \; \text{erfc} \; (s/s_c)$$

$$v_x = -\sqrt{v^2 - v_y^2} \tag{6}$$

where s is arc distance from the bend and the cut-off parameter s_c is given by

$$s_c = \frac{2R}{\sqrt{\pi}} \sin (\theta/2) \tag{7}$$

s_c is adjusted so that the velocity vectors of equations (4), (5) and (6) are identical at the bend axis ($s = 0$ or $\phi = \theta/2$) for small dips. The grid in Fig. 2(b) is constructed so that the sides of the elements are tangent to the velocity vectors (6) imposed on top.

The bottoms of both finite element grids, Fig. 2(a) and (b), are left free: no shear or non-hydrostatic stresses are applied (we do not carry the hydrostatic stresses through the calculation: these are implicitly subtracted at the beginning). The nodes at the ends of each grid are given the velocity of the corresponding topmost node. The grids are long enough that the slight errors induced by this condition do not affect the results (the error is at most 0.01 per cent of the total velocity).

3 The finite element model

We now consider two finite element algorithms for quasi-static non-Newtonian visco-elasticity. We used these algorithms to develop a finite element code to model plate tectonics.

The finite element method enables the modelling of complicated problems in geophysics, but the resulting equations may involve many thousand degrees of freedom. When the problem to be solved is time-dependent and non-linear, the cost can be prohibitive. This has motivated research directed towards developing more efficient computer algorithms for transient non-linear, finite element analysis.

Basically, there are two general classes of algorithms for time-dependent problems; implicit and explicit. Implicit algorithms tend to be numerically stable, permitting large time steps, but the cost per step is high and storage requirements tend to increase dramatically with the size of the mesh. On the other hand, explicit algorithms tend to be inexpensive per step and require less storage than implicit algorithms, but numerical stability requires that small time steps be employed.

With the above in mind, a number of recent papers have described new explicit and implicit algorithms for quasi-static non-Newtonian visco-elasticity. In particular, we have been motivated by the work of Hughes & Taylor (1978) and Cormeau (1975).

Non-Newtonian visco-elasticity can be described by the following constitutive equations:

$$\dot{\epsilon}_{xx} = \frac{(1 + \nu)}{E} \left[(1 - \nu) \dot{\sigma}_{xx} - \nu \dot{\sigma}_{yy} \right] + \frac{\sigma^{n-1}}{4\eta} \left[\sigma_{xx} - \sigma_{yy} \right]$$

$$\dot{\epsilon}_{yy} = \frac{(1 + \nu)}{E} \left[(1 - \nu) \dot{\sigma}_{yy} - \nu \dot{\sigma}_{xx} \right] - \frac{\sigma^{n-1}}{4\eta} \left[\sigma_{xx} - \sigma_{yy} \right] \tag{8}$$

$$\dot{\epsilon}_{xy} = \frac{(1 + \nu)}{E} \dot{\sigma}_{xy} + \frac{\sigma^{n-1}}{2\eta} \sigma_{xy}$$

where

$$\sigma = \sqrt{\left(\frac{\sigma_{xx} - \sigma_{yy}}{2}\right)^2 + \sigma_{xy}^2}.$$

We define the following notation: $\mathbf{B} = \mathbf{B}(x)$ is the strain-displacement matrix, $\mathbf{D} = \mathbf{D}(x)$ is the matrix of elastic properties,

$$\mathbf{K} = \int_\Omega \mathbf{B}^T \mathbf{D} \mathbf{B} \, d\Omega$$

is the stiffness matrix, $\mathbf{F}_N = \mathbf{F}(t_N)$ is the nodal force vector at time t_N, $\mathbf{U}_N = \mathbf{U}(t_N)$ is the nodal displacement vector, and $\sigma_N = \sigma(x, t_N)$ is the stress vector.

$$\begin{bmatrix} \dot{\sigma}_{xx} \\ \dot{\sigma}_{yy} \\ \dot{\sigma}_{xy} \end{bmatrix} = \frac{E}{(1+\nu)(1-2\nu)} \begin{bmatrix} (1-\nu) & \nu & 0 \\ \nu & (1-\nu) & 0 \\ 0 & 0 & (1-2\nu) \end{bmatrix} \left\{ \begin{bmatrix} \dot{\epsilon}_{xx} \\ \dot{\epsilon}_{yy} \\ \dot{\epsilon}_{xy} \end{bmatrix} - \frac{\sigma}{4\eta} \begin{bmatrix} 1 & -1 & 0 \\ -1 & 1 & 0 \\ 0 & 0 & 4 \end{bmatrix} \begin{bmatrix} \sigma_{xx} \\ \sigma_{yy} \\ \sigma_{xy} \end{bmatrix} \right\}$$

or (9)

$$\dot{\boldsymbol{\sigma}} = \mathbf{D}(\dot{\boldsymbol{\epsilon}} - \dot{\boldsymbol{\epsilon}}^{vp}) \tag{10}$$

where

$$\dot{\boldsymbol{\epsilon}}^{vp} = \boldsymbol{\beta}(\boldsymbol{\sigma})$$

$$\dot{\boldsymbol{\epsilon}}^{vp} = \frac{\sigma}{4\eta} \begin{bmatrix} 1 & -1 & 0 \\ -1 & 1 & 0 \\ 0 & 0 & 4 \end{bmatrix} \begin{bmatrix} \sigma_{xx} \\ \sigma_{yy} \\ \sigma_{xy} \end{bmatrix}. \tag{11}$$

The finite element code we developed contains both algorithms described in the Appendix. For the work reported in this paper, we used the implicit algorithm for all linear problems, (i.e. $n = 1$), and the explicit algorithm for all non-Newtonian problems (i.e. $n = 3$). Note that the volume strain, $\epsilon_{xx} + \epsilon_{yy}$, which would normally have to be treated by a penalty function technique for incompressible flow, is handled in a natural way by this code: it remains elastic while the shear strains are governed by viscous flow plus elasticity. The pressure field is thus never decoupled from the rest of the stress tensor and no problems arise in trying to maintain incompressibility. This result is, moreover, closer to reality as well as convenient numerically.

4 Results of the models

4.1 CONSTANT NEWTONIAN VISCOSITY WITH ERROR FUNCTION VELOCITY PROFILE

Fig. 4 shows the results of a typical finite element run for a lithosphere subducting at $45°$ dip with a radius of curvature $R = 1.85 H$ (H = lithosphere thickness) at the bend axis. Grid 2b and boundary conditions (6) are used in this example. The viscosity is assumed to be Newtonian, and is the same in every element. The time dependent calculation is stopped after 50 Maxwell times τ_M ($\tau_M = \eta/G$ where η is the viscosity and G the rigidity of the lower lithosphere), when the viscoelastic transient response of the system has damped out.

Fig. 4(a) is a plot of the vertical stress σ_{yy} on the top of the viscous lower lithosphere. This stress is transmitted through the flexible elastic lithosphere and results in surface
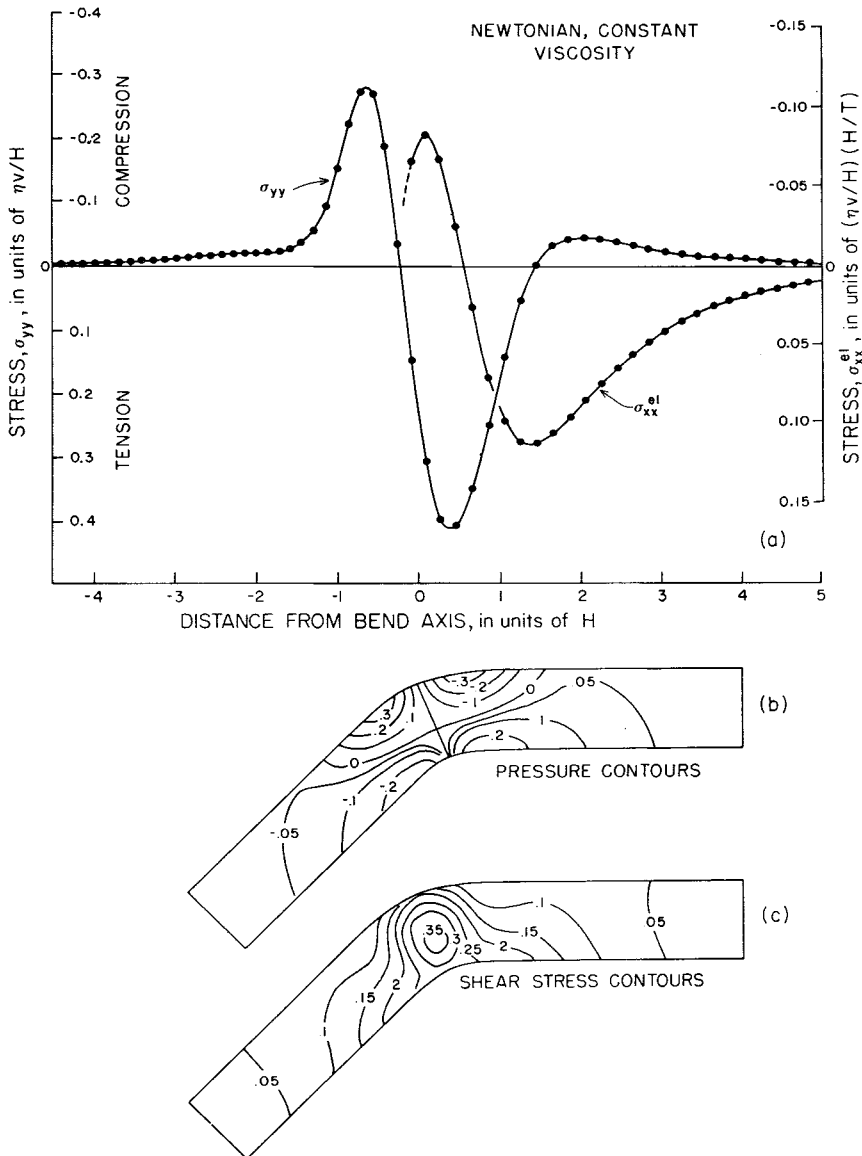
Figure 4. The graphs in the upper half of this figure (part a) show the vertical stress acting on the base of the elastic lithosphere σ_{yy} and the horizontal stress in the elastic lithosphere σ_{xx}^{el} (which must be present to balance shear stresses on its base). The dots on the smooth curves show the location of the centre of the element in which the stress was evaluated. These plots refer to the simple error function velocity profile with radius of curvature $R = 1.85\,H$, dip $45°$, cut-off $s_c = 0.8\,H$. Constant Newtonian viscosity is assumed. Stresses are measured in units of $\eta v/H$, and compressional stresses increase upward so that the σ_{yy} profile models topography. The outer rise is seen on the right of the figure and the trench and island arc form on either side of the bend axis. σ_{xx}^{el} is in extension everywhere seaward of the trench axis. Distances are in units of the lithosphere thickness, H. Contour plots in the lower half of the figure show pressure ($p = -(\sigma_1 + \sigma_2)/2$) and invariant shear stress ($\tau = (\sigma_1 - \sigma_2)/2$) in units of $\eta v/H$. Note the region of low pressure beneath the trench and high pressure near the island arc. A rise in the contours to the right of the trench results in the outer rise. Shear stresses are maximum in the bend axis where they reach values comparable to σ_{yy} in the trench (about $0.4\,\eta v/H$, corresponding to c. 500 bars for a 4.5 km deep trench). The distance scale of these plots is the same as in the graphs of σ_{yy} and σ_{xx}^{el} above, and there is no vertical exaggeration.

topography (equation (1)), as noted on the scale to the left of the figure. Features such as the outer rise, trench, and island arc appear on this plot. All stresses in the model are scaled by the factor $\eta v/H$. Also in Fig. 4(a) is a plot of the extensional stress σ_{xx}^{el} in the elastic lithosphere (equation (3)). As noted previously, this stress is defined only where the upper surface of the lithosphere is free. The sign of this stress agrees with many normal faulting earthquake events in the outer trench region (e.g. 1933 Sanriku Earthquake, Kanamori 1971; 1977 Indonesian Earthquake, Stewart 1978), some of which appear to cut completely through the elastic lithosphere.

Fig. 8(a) shows the direction, magnitudes and sign of the principal stress axes. Lines represent extensional stresses, triangles compressional stresses. Note the region of extension beneath the trench where the lithosphere is in extending flow. Where the lithosphere unbends, shortly after subduction, compressional stresses may be responsible for dynamically maintaining some of the topography (and most of the free air gravity anomaly) of the island arc. The directions of potential fault planes can be estimated from this diagram. Since the bottom of the lithosphere is a free surface, the principal stresses should be either parallel or perpendicular to it. Although Fig. 8(a) shows this to be true in most places, there are some violations of this rule in the bend axis. This occurs because the stresses in the finite element model are evaluated at the *centre* of each element, not on its surface. Thus when stress gradients are high, as in the bend region, the stresses in Fig. 8(a) do not adequately represent the surface stresses. The topography on top of the slab, however, is not much affected by this approximation: various extrapolation schemes were used to relate σ_{yy} on the surface to σ_{yy} at the topmost element midpoints, and less than 1 per cent changes were found.

Fig. 4(b) and (c) is a contour plot of the pressure distribution $p = -(\sigma_1 + \sigma_2)/2$ and invariant shear stress $\tau = (\sigma_1 - \sigma_2)/2$, respectively. σ_1 and σ_2 are principal stresses, using the engineering convention that positive stress is extensional. The relationship between bending and unbending flow in the subducting lithosphere and the pressure distribution is clearly shown in Fig. 4(b), as well as the rise in compression contours that creates the outer rise (which is a reflection of the compressional region in the lowermost part of the lithosphere). Shear stress in the lithosphere reaches a peak at mid-depth near the bend axis. The maximum shear stress is roughly the same size as the pressure deficit under the trench, leading to maximum stress values of a few tens of MPa (hundreds of bars).

The results summarized in Fig. 4(a) refer to a special geometry: dip = 45° and $R = 1.85\,H$. These results can be scaled to any viscosity η, rate of convergence v, and lithosphere thickness H by the parameter $\eta v/H$, but an investigation of the effects of different dips θ and radii of curvature R requires other finite element runs. A number of such runs shows that many features of the stress distribution depend primarily upon the cut-off distance s_c (equation (7)) rather than upon θ or R alone. Fig. 9 shows that the ratio of rise crest height w_b, to trough depth, w_t, depends almost entirely upon s_c/H. Similarly, Fig. 10 shows that rise crest width, x_b/H, trench width, x_t/H, and trench axis to outer wall distance, x_{bt}/H, depend more upon s_c/H than upon dip angle. These figures also show that the finite element results agree very well with the analytic results of Melosh (1978). The largest discrepancy is in Fig. 9 where the ratio w_b/w_t given by the analytical calculation is systematically about 0.03 too large: the outer rise is too high by about 3 per cent of the trench depth. It is not clear whether this is due to the numerical approximations of the finite element code, or to the approximation of the analytical model. The effect is small, however, and in this first order model we do not consider this disagreement of analytical and numerical results to be important.

Fig. 11(a) and (b) demonstrates the dependence of the trench depth and shear stress

upon dip angle and s_c/H: both are important. Note the excellent agreement between the trench depths predicted by the analytic and finite element models at $20°$ dip. The analytic model also predicts the rough linear dependence of trench depth on dip angle, for small angles.

The agreement between the analytic and finite element models using low dips, constant Newtonian viscosity, and the error function velocity profile are evidence that the finite element code works properly. We may apply it with some confidence to situations which cannot be modelled analytically.

4.2 CONSTANT NEWTONIAN VISCOSITY WITH CIRCULAR ARC VELOCITY PROFILE

As Fig. 5 shows, this case is similar to the previous one except for one interesting aspect. The curvature of the error function velocity profile and grid changes smoothly as distance from the bend axis increases. The curvature of the circular arc profile is nearly constant (except for the smoothing function, equation 5) in the bend and zero outside. As a result, lithospheric material which enters the bend is sharply turned down, rotates as a rigid body near the bend axis, then is sharply unbent as it enters the straight dipping section. These regions of sharp bending also account for the apparent narrowness and c. three times greater depth of the trench in Fig. 5(a), compared to Fig. 4(a). Stresses in the region of rigid body rotation near the axis are low: such motion requires no internal deformation of the lithosphere. This fact accounts for the small flat or bench in Fig. 5(a). The development of this bench depends mostly upon dip angle (only a small s_c/H dependence is found). As the angle of dip increases the bench slope increases (the width is nearly constant at about $0.3–0.5\,H$ in our runs with $s_c = 0.8$ and $1.6\,H$ and dips between 10 and $90°$). This small bench usually dips toward the island arc, giving a local reversal of slope. The nature of the bench is reflected by Fig. 5(c), where the shear stress contours show maxima near the ends of the curved section with a saddle point in between, where the lithosphere deforms by simple rotation without distortion.

It is difficult to judge whether any of the well-known benches landward of oceanic trenches (Hayes & Ewing 1970) are due to this mechanism. Such benches are usually interpreted as accretionary prisms (Karig 1974), and we know of no evidence that *requires* dynamical support. The actual profiles of subducting slabs (whether they are best approximated by the grid of Fig. 2(a) or (b)) are not well enough known to resolve this subtle question. We thus leave it as an interesting but unproven speculation that a part of the topography and gravity anomalies associated with these benches may be of dynamical origin. The resolution of this issue could be important for the sedimentary history of the trench, since the backward-sloping portion of the bench acts as a sediment trap. Increases of convergence rate or angle of subduction deepen this trap, so that perhaps correlations between these variables and sedimentary history are possible.

4.3 DEPTH DEPENDENT NEWTONIAN VISCOSITY

A realistic description of the rheology of the lithosphere must allow its viscosity to decrease with depth. In reality, the viscosity probably varies from about $10^{26}\,P$ at the base of the elastic lithosphere (corresponding to a Maxwell time of a few Myr) to $10^{21}\,P$ or less in the asthenosphere. This magnitude of viscosity variation is too great for our numerical methods to retain both stability and accuracy, so we report here on the qualitative results of a much smaller viscosity variation. We used an error function velocity profile (equation (6)) and
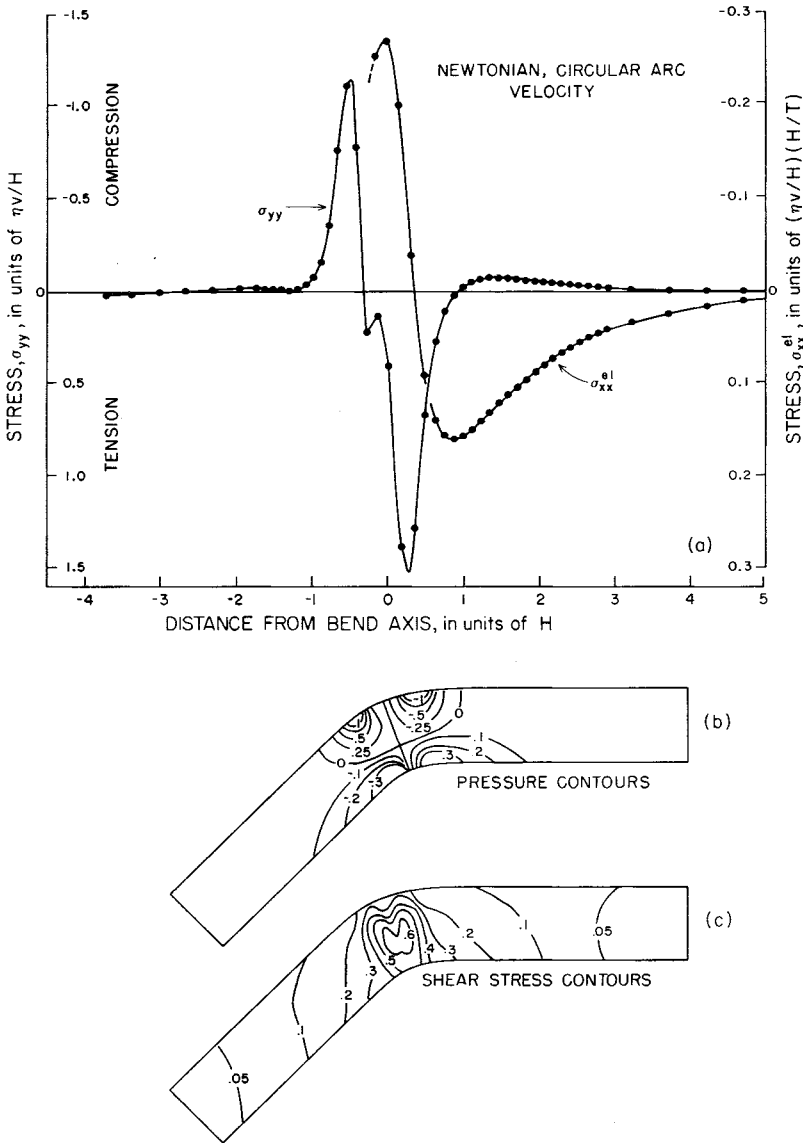
Figure 5. Same as Fig. 4, except that the stresses are plotted for the circular arc profile. Radius of curvature $R = 1.85 H$, dip $\theta = 45°$, cut-off $s_c = 0.8 H$, and constant Newtonian viscosity are assumed. Note the concentration of shear stress into two maxima, one at the beginning and one at the end of the bend. This is reflected by the bench which forms in the σ_{yy} profile. The trench which forms in this case is narrower and about three times deeper than for the error function profile in Fig. 4 (note the scale changes). The stresses in the elastic slab σ_{xx}^{el}, however, are nearly the same size as those in Fig. 4.

grid (Fig. 2(b)) dipping at 10 and 45° with a variety of R (yielding $s_c/H = 0.4, 0.8$ and 1.2). In these runs we allowed the viscosity of the topmost of the five elements in the lithosphere to be either 2.5 times or 50 times the viscosity of the lowest element. The viscosities of the intermediate elements were determined by linear interpolation of these extremes. Fig. 6(b) and (c) shows the pressure and shear stress contours for 45° dip, $R = 1.85 H$, and 50 times viscosity variation: a marked displacement toward the upper (high viscosity) layers is seen.
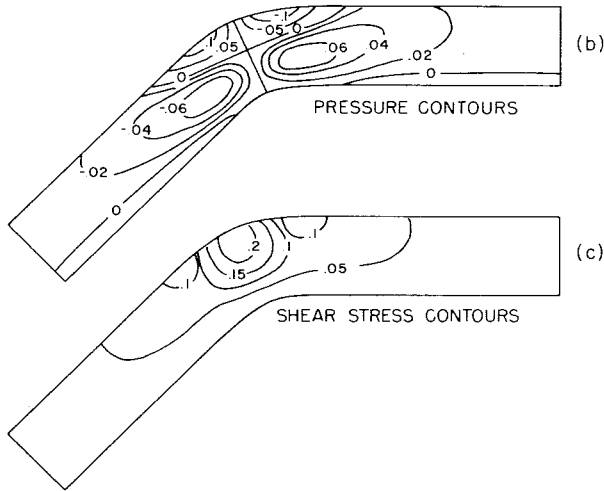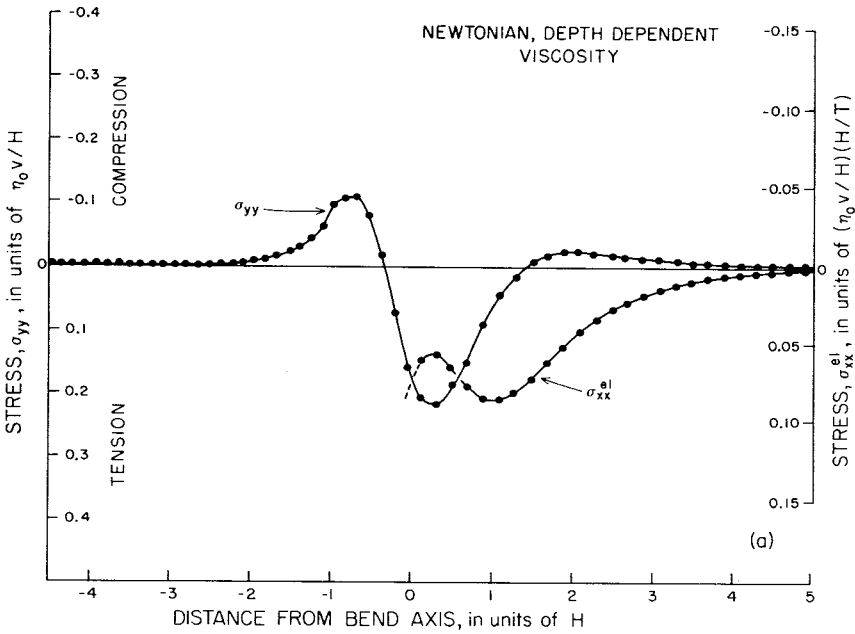
Figure 6. Same as Fig. 4, with $R = 1.85\,H$, $\theta = 45°$, $s_c = 0.8\,H$, and depth dependent Newtonian viscosity. The viscosities of the five layers of elements are, from the top down, 50, 37.75, 25.5, 12.75 and 1. An error function velocity profile is applied. Note the concentration of shear stress and pressure contours toward the top and the generally lower stress values. Otherwise, the σ_{yy} profile shows no strong effects of the viscosity dependence. Stresses are in units of $\eta_0 v/H$, where η_0 is the viscosity of the topmost element.

Figs 9 and 10 show that the rise crest height/trench depth ratio, the rise crest widths, and the trench width are very similar to the analytic and constant viscosity results for all runs. Evidently even a 50 times viscosity decrease does not significantly affect the geometry of the resulting trench and outer rise. The trench depth and shear stress in Fig. 11(a) and (b) depend more strongly upon the viscosity variation (when normalized by the topmost layer viscosity, $\eta_0 v/H$). These results are summarized by a simple rule of thumb: if the viscosity
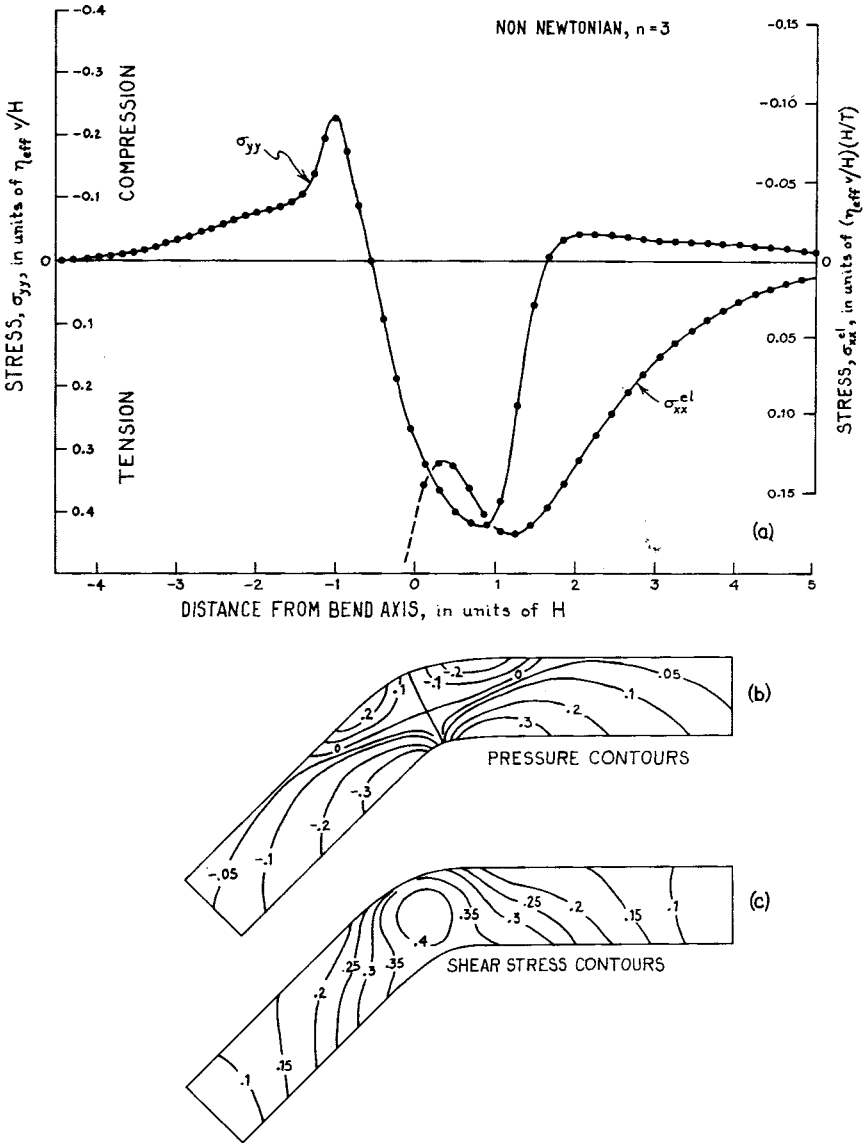
Figure 7. Same as Fig. 4, with $R = 1.85\,H$, $\theta = 45°$, $s_c = 0.8\,H$, and non-Newtonian ($n = 3$) viscosity. An error function velocity profile is applied. The trench is broader, more U-shaped and asymmetric than the Newtonian profiles. σ_{xx}^{el} is extensional a considerable distance down the slab. The shear stress contours lack the concentrated maximum shown by Newtonian viscosity lithospheres. Stresses are in units of $\eta_{eff}v/H$, where η_{eff} is the effective viscosity at the highest shear stress.

depends linearly upon depth, the effective viscosity of the lithosphere is $\eta_{eff} \approx \eta_0/2$ when the viscosity of the topmost elements is more than a few times the viscosity of the lowest elements. This rule applies best for the strong, 50 times, viscosity variation.

4.4 NON-NEWTONIAN RHEOLOGY

An increasing amount of evidence, both theoretical and experimental (Weertman & Weertman 1975) and geophysical (Melosh 1976) suggests that the rheology of the mantle is non-
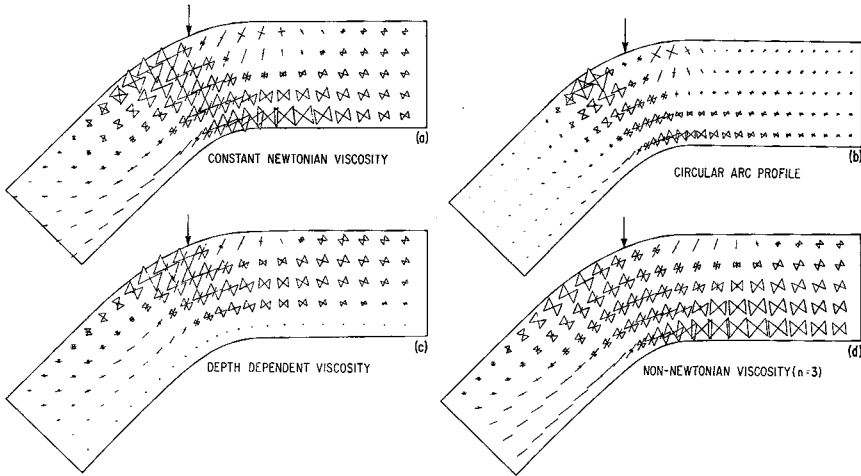
Figure 8. Plots (a), (b), (c) and (d) refer, respectively, to the stresses in the lithosphere for Figs 4, 5, 6 and 7. These plots show the sign, magnitude and directions of the principal stresses in the bending lithosphere. The triangular symbols show the direction of compressional principal stresses, lines represent extensional principal stresses, and the size of the symbol is proportional to the magnitude of the stress. The vertical arrows show the positions of the bend axes.

Newtonian. The flow law seems to be adequately described as a power law of the form

$$\dot{\epsilon}_{ij}|_{\text{steady state}} = \frac{1}{2\eta_n} \sigma^{n-1} \sigma_{ij} \tag{12}$$

where η_n is a constant (it is identical to viscosity for $n = 1$), and σ is the second stress invariant. A useful way of rewriting equation (12) is

$$\dot{\epsilon}_{ij}|_{\text{steady state}} = \left(\frac{1}{2\eta_{\text{eff}}}\right) \sigma_{ij} \tag{13}$$

where

$$\eta_{\text{eff}} \equiv \eta_n / \sigma^{n-1} \tag{14}$$

is an 'effective' viscosity which is stress dependent. The larger the stress σ, the smaller the effective viscosity becomes. Large stresses may thus make the mantle more fluid.

Section 3 discussed the finite element code and the computation of the non-Newtonian rheology. Fig. 7 is a plot of the stresses developed in a subducting slab using the error function velocity profile (6) and grid (Fig. 2(b)). The power law is assumed to be $n = 3$, and η_3 does not depend upon depth. The general features of Fig. 7 are much like the Newtonian viscosity case, except that the trench is somewhat wider than that of the corresponding Newtonian rheology (Fig. 5), more U-shaped, and more asymmetric. Figs 9 and 10 show the remarkable similarity of the non-Newtonian and Newtonian topographic profiles, for dips of 10 and 45° and $s_c = 0.80H$. Even more remarkable is the dependence of trench depth and shear stress on dip angle, Fig. 11(a) and (b). The non-Newtonian and Newtonian results are virtually identical, once stresses are normalized by $\eta_{\text{eff}} v/H$, where η_{eff} is defined as $\eta_3/\sigma_{\text{max}}^2$, and σ_{max} is the maximum shear stress (occurring near the bend axis). Dimensional analysis indicates that η_{eff} should only depend upon the combination

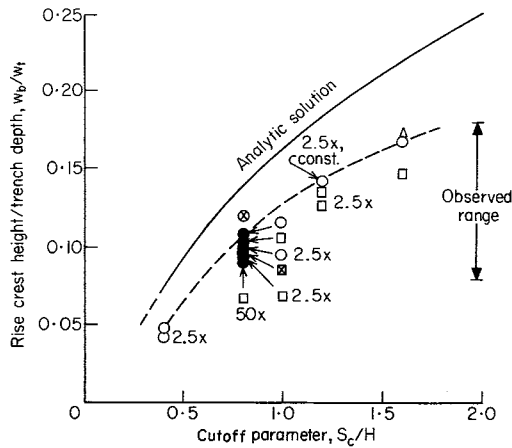$$N = \left(\frac{\eta_3 H^2}{v^2 \sin^2 \theta}\right)^{1/3}$$

Figure 9. Rise crest height divided by trench depth, w_b/w_t, is plotted versus cut-off parameter s_c/H for error function velocity profiles with a variety of dips, non-Newtonian viscosity and depth-dependent viscosity. The observed range of w_b/w_t from Table 1 is also indicated. The value of w_b/w_t evidently depends more upon s_c/H than dip. The most serious discrepancy between the numerical results and the approximate analytic model of Melosh (1978) is shown in this plot. Note, however, that the discrepancy in outer rise height is only 3 per cent of the trench depth. Points resulting from depth dependent Newtonian viscosities are indicated by 2.5 X or 50 X symbols, denoting the magnitude of the viscosity variation. Key: ○ − 10° dip, Newtonian viscosity; ◻ − 45° dip, Newtonian viscosity; △ − 90° dip, Newtonian viscosity; ⊗ − 10° dip, $n = 3$; ⊠ − 45° dip, $n = 3$.
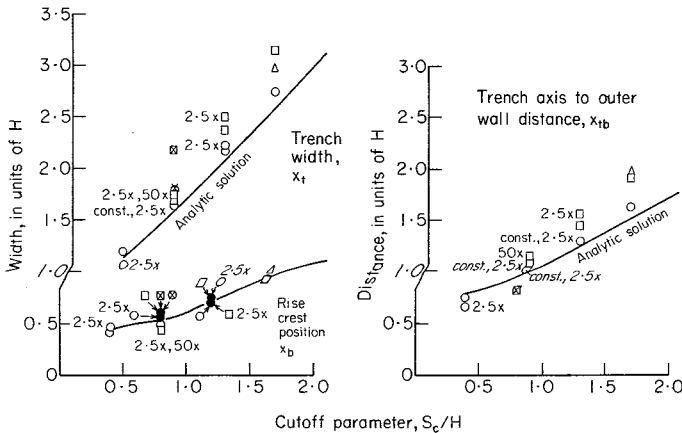

Figure 10. Trench width x_t and x_{tb} and outer rise crest position x_b (see Fig. 1) as a function of s_c/H and dip for a variety of error function velocity profiles. Note the lack of strong dependence on dip and the excellent agreement of analytic and numerical results. Key as in Fig. 9.

a relation which seems to hold roughly for our calculations, where $\eta_{eff} = 1.62 N$, $1.65 N$ and $1.37 N$ was found for $s_c = 0.80 H$ and $\theta = 10$, 25 and 45°. We assumed $\eta_3 = 10^{-9}$, $v = 4 \times 10^{-5}$ and $H = 1$ in our computer runs.

Note that a non-Newtonian rheology with very large n can be approximated by a perfectly plastic substance (Paterson 1969, p. 87). It is thus interesting to note that Lobkovsky (1976) obtained results very similar to ours in his study of the bending of a perfectly plastic lithosphere. Turcotte, MacAdoo & Caldwell (1978) also obtained an adequate fit to the outer rise with an elastic-perfectly plastic model. However, both require
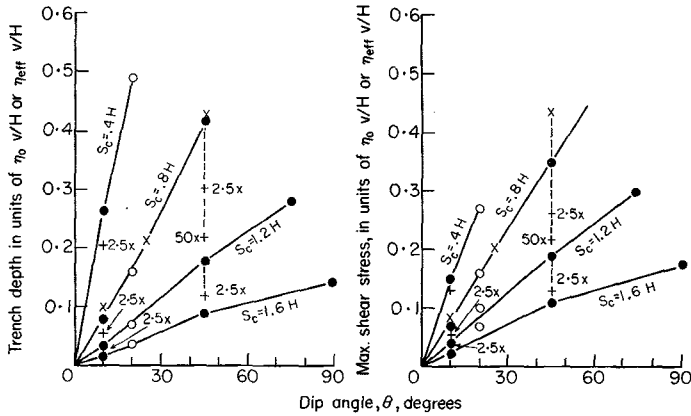
Figure 11. (a) Shows the trench depth versus dip in units of $\eta_0 v/H$, or $\eta_{eff} v/H$ for constant Newtonian, depth dependent Newtonian, and non-Newtonian viscosities, respectively. The depth of the trench is a function both of dip and s_c. The analytic and numerical results are in excellent agreement. Dashed vertical lines connect results for depth dependent viscosities with the corresponding constant viscosity results (i.e. same s_c/H). (b) Compares maximum shear stress (in the same units as (a)) to dip and s_c. The numerical and analytical results do not agree so well for this case, and there is more scatter in the results for constant Newtonian, depth dependent Newtonian, and non-Newtonian viscosities. Key: ● – constant Newtonian viscosity; X – non-Newtonian, $n = 3$; + – depth-dependent Newtonian; ○ – analytical solution.

very large stresses (kilobars or more) to support the outer rise, a feature which they share with the thin plate elastic flexure models (Hanks 1971).

Although more work could be done on the non-Newtonian rheology, the similarity of these results to the results of a Newtonian rheology (once stresses are correctly normalized) makes the graphs reported in Figs 9–11 immediately useful for first-order application to the Earth.

5 Discussion

The preceding finite element analysis shows that neither depth dependent viscosity nor non-Newtonian rheology alters the essential results of the analytic model of Melosh (1978). The circular-segment velocity boundary condition shows that flats or benches between the trench and island arc may owe some of their topography to dynamic forces.

The principal result of this work is that the first order topographic features of a subduction zone can be explained by viscous stresses generated in the lower lithosphere during subduction. Deviatoric stresses of a few tens of MPa (hundreds of bars) can support the outer rise. These results are in substantial agreement with those of Sleep (1975), who studied a fluid dynamical model of the entire subduction zone. Our work, however, has shown that the stress in the lithosphere and the topography of the subduction zone depend principally upon the geometry of the dipping slab and the effective viscosity in the bend region. The detailed dynamics of the subduction zone determine this geometry, of course, but it is important to realize that once the geometry (dip, radius of curvature) is established, the topography of the subduction zone is not very sensitive to the rheology. Study of the topography of subduction zones thus gives little data about rheology, except for the effective viscosity.

Table 1 presents numerical data on several trenches from Caldwell *et al.* (1976). The key parameter from this data is the ratio w_b/w_t, rise crest height/trough depth. The observed

Table 1. Subduction zone data.

Location	Rise Crest[a] Height, w_b	Trench Depth, w_t	Trench Axis– Outer Wall Distance x_{tb}	Rise Crest[a] Position x_b	Convergence† Velocity, v	Dip††	Ratio[a] w_b/w_t	Cutoff[b] Parameter s_c/H	Viscous[c] Lithosphere Thickness H	Effective[d] Viscosity η_{eff}
Bonin Trench* $30°$–$34°$ N										
A	.40km	2.86km	58km	55km	6.1 cm/yr	$60°$	.14	1.35±.15	38±4km	5×10^{22} poise
B	.39	3.22	65	49	6.3	$60°$	.12	1.0±.1	52±5	4×10^{22}
C	.40	2.86	76	32	6.5	$60°$	.14	1.35±.15	50±5	7×10^{22}
D	.29	3.36	66	52	6.7	$60°$	.09	.75±.05	63±10	3×10^{22}
E	.53	3.00	58	41	6.9	$60°$	.18	2.2±.4	27±5	12×10^{22}
Mariana*	.50	3.59	71	55	3.0	$81°$	.14	1.35±.15	48±5	13×10^{22}
Bonin*	.40	2.87	70	53	6.5	$60°$	.14	1.35±.15	47±5	6×10^{22}
Aleutian*	.35	2.05	58	53	8.0	$67°$	.17	2.0±.3	29±5	7×10^{22}
Kuril*	.28	2.43	68	42	10.0	$56°$	.12	1.0±.1	47±5	2×10^{22}
Peru–Chile ($23°$ S)**	.20	2.48	64	50(?)	9.3	$30°$	.08	.70±.05	62±10	2×10^{22}

Mean: 6×10^{22}

* Geometrical data (w_b, w_t, x_{tb}, and x_b) from Caldwell et al. (1976).

** Geometrical data from Hayes and Ewing (1970); uncorrected seismic profiler trace.

† Computed from data in Minster and Jordan (1979) and Seno (1977).

†† From Tovish and Schubert (1978).

(a) These parameters are difficult to measure and thus highly uncertain--perhaps by as much as a factor of two.
(b) Computed from Fig. 9. Uncertainty reflects scatter in numerical results only; no account is taken of errors in w_b.
(c) Computed from s_c/H and x_{tb}, using Fig. 10.
(d) These values are very uncertain--they should be considered order-of-magnitude estimates only.

range corresponds well (Fig. 9) with a range of cut-off parameters $s_c \approx 0.6-2.0H$ (for the numerical solutions). Fig. 10 shows that this range in s_c implies trench widths of 1.4 to $3.0H$, or 100 to 210 km for $H = 80$ km thick lithosphere. Similarly, the rise crest position should range from 35 to about 80 km. Table 1 shows that these ranges are reasonably accurate for observed trenches. Note, however, that some quantities (especially the rise crest width) are subject to very large uncertainties. Figs 9 and 10 are used to determine the lithosphere thickness from w_b/w_t and the trench axis to outer wall distance x_{tb}. Lithospheric thicknesses scatter a great deal, but one must remember that small errors in w_b can lead to large errors in H. Obviously, careful modelling is required before firm values of the lithosphere thickness can be quoted. The thicknesses obtained, however, are not unreasonable for the viscous lower lithosphere. The mean value of c. 50 km, when supplemented by a 20 km thick elastic lithosphere, sum to the c. 70 km thickness of old oceanic (seismic) lithosphere.

Effective viscosity is computed using Fig. 11, the convergence rates of Minster & Jordan (1979), and dips of Tovish & Schubert (1978). Lithosphere thicknesses H are taken from the previous calculation. Most subduction zones show an effective viscosity η_{eff} between about 2×10^{22} and 10^{23} P, with a mean of 6×10^{22} P. This value is lower than most previous estimates for mid-depth in the lithosphere (Weertman & Weertman 1975; Murrell 1976). However, the results on non-Newtonian flow show that this must be interpreted as an effective viscosity at a stress equal to the maximum shear stress in the bend region, which in turn nearly equals the stress creating the trench (several tens of MPa; Fig. 11(a) and (b)). The low effective viscosity is thus explained if the rheology of the lithosphere is non-Newtonian, a result which seems particularly likely at the large stresses involved (Stocker & Ashby 1973; Schwenn & Goetze 1978).

Acknowledgments

References

Batchelor, G. K., 1970. *Introduction to Fluid Dynamics*, Cambridge University Press, Cambridge.

Caldwell, J. G., Haxby, W. F., Karig, D. E. & Turcotte, D. L., 1976. On the applicability of a universal elastic trench profile, *Earth planet. Sci. Lett.*, 31, 239–246.

Chapple, W. M. & Forsyth, D. W., 1979. Earthquakes and bending of plates at trenches, *J. geophys. Res.*, in press.

Chinnery, M. A., 1964. The strength of the Earth's crust under horizontal shear stress, *J. geophys. Res.*, 69, 2085–2089.

Cormeau, I. C., 1975. Numerical stability in quasi-static elasto/visco-plasticity, *Int. J. numer. Meth. Engng*, 9, 109–127.

Davies, G. F. & Brune, J. N., 1971. Regional and global fault slip rates from seismicity, *Nature Phys. Sci.*, 229, 101–107.

Elsasser, W. M., 1969. Convection and stress propagation in the upper mantle, in *The Application of Modern Physics to the Earth and Planetary Interiors*, pp. 223–246, ed. Runcorn, S. K., Wiley & Sons, New York.

Hanks, T. C., 1971. The Kuril trench–Hokkaido rise system: Large shallow earthquakes and simple models of deformation, *Geophys. J. R. astr. Soc.*, 23, 123–189.

Hayes, D. E. & Ewing, M., 1970. Pacific boundary structure, in *The Sea*, pp. 29–72, ed. Maxwell, A. E., Wiley & Sons, New York.

Hughes, T. J. R. & Taylor, R. L., 1978. Unconditionally stable algorithms for quasi-static elasto/visco-plastic finite element analysis, *Comput. Struct.*, 8, 169–173.

Jones, G. M., Hilde, T. W. C., Sharman, G. F. & Agnew, D. C., 1979. Fault patterns in outer trench walls and their tectonic significance, *J. Phys. Earth*, in press.

Karig, D. E., 1974. Evolution of arc systems in the western Pacific, *A. Rev. Earth planet. Sci.*, 2, 51–75.

Kanamori, H., 1971. Seismological evidence for a lithospheric normal faulting: The Sanriku earthquake of 1933, *Phys. Earth planet. Interiors*, 4, 289–300.

Lobkovsky, L. I & Sorokhtin, O. G., 1976. Plastic deformations of the oceanic lithosphere in the sub-duction zone (in Russian), in *Tektonika Litosferic Plit (Denamika Zoni Poddviga)*, pp. 22–52, Akad. Nauk SSSR, Moskva.

McNutt, M. & Menard, H. W., 1978. Lithospheric flexure and uplifted atolls, *J. geophys. Res.*, 83, 1206–1212.

Melosh, H. J., 1976. Nonlinear stress propagation in the Earth's upper mantle, *J. geophys. Res.*, 81, 5621–5632.

Melosh, H. J., 1977. Shear stress on the base of a lithospheric plate, *Pure appl. Geophys.*, 115, 429–439.

Melosh, H. J., 1978. Dynamic support of the outer rise, *Geophys. Res. Lett.*, 5, 321–324.

Minster, J. B. & Jordan, T. H., 1978. Present-day plate motions, *J. geophys. Res.*, 83, 5331–5354.

Murrell, S. A. F., 1976. Rheology of the lithosphere – experimental indications, *Tectonophysics*, 36, 5–24.

Officer, C. B., 1974. *Introduction to Theoretical Geophysics*, p. 367, Springer, New York.

Paterson, W. S. B., 1969. *The Physics of Glaciers*, Pergamon Press, Oxford.

Schwenn, M. B. & Goetze, C., 1978. Creep of olivine during hot-pressing, *Tectonophysics*, 48, 41–60.

Seno, T., 1977. The instantaneous rotation vector of the Philippine Sea plate relative to the Eurasia plate, *Tectonophysics*, 42, 209–226.

Sleep, N. H., 1975. Stress and flow beneath island arcs, *Geophys. J. R. astr. Soc.*, 42, 827–857.

Stewart, G. S., 1978. Implications for plate-tectonics of the August 19, 1977 Indonesian decoupling normal-fault earthquake, *EOS, Trans. Am. geophys. Un.*, 59, 326.

Stocker, R. L. & Ashby, M. F., 1973. On the rheology of the upper mantle, *Rev. Geophys. Space Phys.*, 11, 391–426.

Tovish, A. & Schubert, G., 1978. Island arc curvature, velocity of convergence and angle of subduction, *Geophys. Res. Lett.*, 5, 329–332.

Turcotte, D. L., MacAdoo, D. C. & Caldwell, J. G., 1978. An elastic-perfectly plastic analysis of the bending of the lithosphere at a trench, *Tectonophysics*, 47, 193–205.

Walcott, R. I., 1970. Flexural rigidity, thickness and viscosity of the lithosphere, *J. geophys. Res.*, 75, 3941–3954.

Watts, A. B., 1978. An analysis of isostasy in the world's oceans. 1. Hawaiian-Emperor Seamount Chain, *J. geophys. Res.*, 83, 5989–6004.

Watts, A. B., Cochran, J. R. & Selzer, G., 1975. Gravity anomalies and flexure of the lithosphere: A three-dimensional study of the Great Meteor Seamount, Northeast Atlantic, *J. geophys. Res.*, 80, 1391–1398.

Watts, A. B. & Talwani, M., 1974. Gravity anomalies seaward of deep-sea trenches and their tectonic implications, *Geophys. J. R. astr. Soc.*, 36, 57–90.

Weertman, J. & Weertman, J. R., 1975. High temperature creep of rock and mantle viscosity, *A. Rev. Earth Planet. Sci.*, 3, 293–315.

Appendix

Following Cormeau (1975), we define an explicit algorithm for equation (8) as follows:

1. Initialization

   (a) form $\mathbf{K}_0$ and $\mathbf{F}_0$

   (b) decompose $\mathbf{K}_0$ into $\mathbf{LDL}^T$

   (c) solve for $\mathbf{U}_0$

   (d) $\boldsymbol{\sigma}_0 = \mathbf{DBU}_0$, $\quad \boldsymbol{\epsilon}_0^{vp} = 0$.

2. Define

   $$\boldsymbol{\epsilon}_{N+1}^{vp} = \boldsymbol{\epsilon}_N^{vp} + \Delta t \boldsymbol{\beta}(\boldsymbol{\sigma}_N).$$

12

3. Form

$$\mathbf{F}_{N+1}.$$

4. Back-substitute to find $\mathbf{U}_{N+1}$

$$(\mathbf{LDL}^T)\mathbf{U}_{N+1} = \int_\Omega \mathbf{B}^T\mathbf{D}\boldsymbol{\epsilon}^{vp}_{N+1}\, d\Omega + \mathbf{F}_{N+1}.$$

5. $\boldsymbol{\sigma}_{N+1} = \mathbf{D}(\mathbf{BU}_{N+1} - \boldsymbol{\epsilon}^{vp}_{N+1}).$

6. Set $N = N + 1$, if

$$\sum_{i=1}^{N} \Delta t_i < T,$$

go to 2; otherwise stop.

T is the time interval over which the calculation is to be performed. Defining: $\mathbf{S} = \mathbf{D}^{-1}$, $\boldsymbol{\beta}'$ is the Jacobian matrix formed by differentiating $\boldsymbol{\beta}$ with respect to the components of $\boldsymbol{\sigma}_N$ and $\mathbf{U}_{N+1} = \delta\mathbf{U}_{N+1} + \mathbf{U}_N$, $\boldsymbol{\sigma}_{N+1} = \delta\boldsymbol{\sigma}_{N+1} + \boldsymbol{\sigma}_N$.

Hughes & Taylor (1978) considered the following implicit algorithm, where $\alpha\epsilon\,[0, 1]$

1. Initialization

   (a) form $\mathbf{K}_0$ and $\mathbf{F}_0$
   (b) decompose $\mathbf{K}_0$ into $\mathbf{LDL}^T$
   (c) solve for $\mathbf{U}_0$
   (d) $\boldsymbol{\sigma} = \mathbf{DBU}_0.$

2. Form

$$K_{N+1} = \int_\Omega \mathbf{B}^T(\mathbf{S} + \alpha\Delta t\boldsymbol{\beta}'_N)^{-1}\mathbf{B}\, d\Omega$$

$$\mathbf{F}_{N+1} = \int \mathbf{B}^T(\mathbf{S} + \alpha\Delta t\boldsymbol{\beta}'_N)^{-1}(\Delta t\boldsymbol{\beta}_N)\, d\Omega + \mathbf{F}_{N+1}.$$

3. Solve $\mathbf{K}_{N+1}\delta\mathbf{U}_{N+1} = \mathbf{F}_{N+1}.$

4. $\delta\boldsymbol{\sigma}_{N+1} = (\mathbf{S} + \alpha\Delta t\boldsymbol{\beta}'_N)^{-1}(\mathbf{B}\delta\mathbf{U}_{N+1} - \Delta t\boldsymbol{\beta}_N).$

5. Update

$$\mathbf{U}_{N+1} = \mathbf{U}_N + \delta\mathbf{U}_{N+1}$$

$$\boldsymbol{\sigma}_{N+1} = \boldsymbol{\sigma}_N + \delta\boldsymbol{\sigma}_{N+1}.$$

6. Set $N = N + 1$, if

$$\sum_{i=1}^{N} \Delta t_i < T,$$

go to step 2; otherwise stop.